Scanning Electron Microscopy

Volume 1982
Number 1 *1982*

Article 19

1982

Electron Energy Loss Microspectroscopy and the Characterization of Solids

Richard Leapman
National Institutes of Health

Follow this and additional works at: https://digitalcommons.usu.edu/electron

Part of the Biology Commons

Recommended Citation

Leapman, Richard (1982) "Electron Energy Loss Microspectroscopy and the Characterization of Solids," *Scanning Electron Microscopy*: Vol. 1982 : No. 1 , Article 19.
Available at: https://digitalcommons.usu.edu/electron/vol1982/iss1/19

This Article is brought to you for free and open access by the Western Dairy Center at DigitalCommons@USU. It has been accepted for inclusion in Scanning Electron Microscopy by an authorized administrator of DigitalCommons@USU. For more information, please contact digitalcommons@usu.edu.

Electron Beam Interactions With Solids (Pp. 217-233)
SEM, Inc., AMF O'Hare (Chicago), IL 60666, U.S.A.

ELECTRON ENERGY LOSS MICROSPECTROSCOPY AND THE CHARACTERIZATION OF SOLIDS

RICHARD LEAPMAN
Biomedical Engineering and Instrumentation Branch, Bldg. 13, Room 3W13
National Institutes of Health
Bethesda, MD 20205
Tel: (301) 496-2599

ABSTRACT

The inelastic scattering of fast electrons provides a detailed means of characterizing the chemical composition and electronic properties of thin samples in an electron microscope. Collective and single-electron excitations occuring in the low energy region of the spectrum can be described in terms of the generalized dielectric formulation. Important information is contained in this part of the spectrum but some prior detailed knowledge of the sample is usually required for proper interpretation. The core excitations allow microanalytical information to be obtained and quantitative procedures are now quite well developed at least for K and L edges. Sample thickness is one factor that limits the quality of data in energy loss spectra and it is now possible to remove the effects of plural scattering from core edges as well as from the low loss spectrum. Several advances in instrumentation have been made recently both in electron optics and recording devices. It appears that the detection limits are very low, possibly 1 to 10 atoms in an optimized system. Measurements also show that the core edges offer a sensitive method for probing the chemical bonding and electronic structure, provided the energy resolution is sufficient (≤ 1 eV). Of particular interest is the momentum transfer and orientation dependence of the fine structure for crystalline materials. The transition elements exhibit very sharp features near the L_{23} threshold due to transitions to unoccupied d states and reasonable agreement is found with theory here. Another type of information can be obtained from the extended fine structure above the core edges (EXELFS). This is capable of yielding the local atomic environment around the different atomic species.

Keywords: Electron energy loss spectroscopy, microanalysis, dielectric constant, core edges, fine structure, extended energy loss fine structure (EXELFS), quantitation, plural scattering, chemical bonding, detection limits, electron spectrometers, valence electron excitations, orientation dependence.

INTRODUCTION

The purpose of this paper is to present a survey of the current state-of-the-art in electron energy loss spectroscopy as applied to electron microscopy and to identify which aspects of the subject are not fully understood or developed. Inelastic scattering of fast electrons gives considerable information about the chemical and electronic structure of a solid. When combined with the high spatial resolution of the electron microscope it offers a powerful probe on a nanometer scale.

Inelastic scattering processes can be broadly divided into two types, those which involve relatively small transfers of energy to the sample, i.e., less than about 50 eV (valence electron excitations), and those which involve larger energy transfers, typically some hundreds of eV (core excitations). Much of the earlier work in the field was spent exploiting both types of excitation (Hillier and Baker, 1944; Watanabe, 1955; Castaing and Henry, 1962; Wittry et al., 1969; Curtis and Silcox, 1971; Isaacson, 1972; Colliex and Jouffrey, 1972; Egerton and Whelan, 1974a; Williams and Edington, 1976).

Recently however interest has largely centered on the core excitations, at least as far as the electron microscopist is concerned (Isaacson and Johnson, 1975; Colliex et al., 1976; Egerton, 1978; Joy, 1979; Maher, 1979; Krivanek, 1980). This has been mainly because the core edges give information about elemental composition especially for the low Z elements where the conventional x-ray microprobe is least sensitive. By comparison the low loss spectrum is generally not characteristic of the elements present in the sample (Daniels et al., 1970). Moreover it has been established that the core edge fine structure can be analyzed to probe the chemical bonding and energy bands in a sample and that this is often less difficult to interpret than the structure at low energy losses (Colliex and Jouffrey, 1972; Isaacson, 1972; Egerton and Whelan 1974c; Leapman and Silcox, 1979). Nevertheless, excitations of the valence electrons contain a wealth of detailed information which should prove very valuable, especially with more sophisticated instrumentation and methods of data analysis (Silcox, 1978). Although we shall concentrate here chiefly on the higher energy loss processes, i.e., core edges, a general description of the spectrum will also be given to include the valence excitations.

LIST OF SYMBOLS

$\hbar$	= Planck's constant/2π.
m	= Rest mass of the electron.
e	= Charge of the electron.
E_0	= Incident electron energy.
$\underline{v}$	= Incident electron velocity.
$\underline{k}$	= Wavevector of incident electron.
$\underline{k}'$	= Scattered electron wavevector.
$\underline{q}$	= Momentum transfer.
$\underline{r}$	= Electron position vector.
E	= Energy loss.
$q_{//}$	= Momentum transfer parallel to beam direction.
$q_{\perp}$	= Momentum transfer perpendicular to beam direction.
Θ	= Scattering angle.
Θ_E	= Characteristic scattering angle.
σ	= Cross section.
Ω	= Solid angle.
a_0	= Bohr radius of atom.
$S(\underline{q},E)$	= Dynamical form factor.
$\hbar\omega_p$	= Plasmon energy.
n	= Electron density.
$\epsilon(\underline{r},t)$	= Dielectric constant.
$\epsilon(\underline{q},E)$	= Dielectric constant.
Im	= Imaginary part.
ϵ_1	= Real part of dielectric constant.
ϵ_2	= Imaginary part of dielectric constant.
$\|i>$	= Initial state wavefunction.
$\|f>$	= Final state wavefunction.
$\frac{df}{dE}(\underline{q},E)$	= Differential generalized oscillator strength.
$\hat{\epsilon}_q$	= Unit vector in direction of $\underline{q}$.
$\Delta\ell$	= Change in angular momentum quantum number.
r_c	= Core wavefunction radius.
I(E)	= Energy loss intensity distribution.
N(E)	= Density of unoccupied states.
P(E)	= Matrix element factor.
D	= Spectrometer energy dispersion.
R	= Spectrometer bending radius.
C	= Aberration coefficient of spectrometer.
γ	= Spectrometer acceptance angle.
$\propto$	= Collection angle for scattering at sample.
M	= Image magnification.
t	= Sample thickness.
$I_0(E)$	= Instrumental resolution function.
Q(E)	= Single scattering distribution.
$Q(E,\Theta)$	= Single scattering distribution.
λ_T	= Total inelastic mean free path.
I_T	= Total area under spectrum.
I_Z	= Area under zero loss peak.
S_X	= Signal counts at core edge for element X.
N_X	= Number of atoms X per unit area.
τ	= Integration time.

LIST OF SYMBOLS

J	= Probe current.
Δ	= Energy window above edge.
$\frac{dB}{dE}$	= Number of background counts per unit energy loss.
A	= Constant for inverse power law of background.
r	= Exponent for inverse power law of back-background.
$\eta(\propto)$	= Angular collection efficiency.
$\eta(\Delta)$	= Energy window collection efficiency.
σ_T	= Total cross section for ionization of core level.
Θ_{max}	= Maximum cut-off scattering angle.
$\sigma_X(\propto,\Delta)$	= Partial cross section for angle $\propto$ and energy window Δ.
$S_X(\propto,\Delta)$	= Measured integrated signal in core edge for angle $\propto$ and energy window Δ.
$I(\propto,\Delta)$	= Measured integrated intensity in low loss spectrum for angle $\propto$ up to energy Δ.
L(E)	= Low loss intensity distribution.
i(e)	= Fourier transform of I(E).
$i_0(e)$	= Fourier transform of $I_0(E)$.
$\ell(e)$	= Fourier transform of L(E).
F^{-1}	= Inverse Fourier transform.
Q′(E)	= Broadened single scattering distribution.
δE	= Energy channel width.
δS	= Signal in one channel.
δB	= Background in one channel.
N_B	= Number of matrix atoms per unit area contributing to the background.
$\frac{d\sigma_X}{dE}$	= Differential cross section for core loss.
$\frac{d\sigma_B}{dE}$	= Differential cross section for background due to matrix.
b	= Impact parameter.
k	= Wavevector of ejected electron.
E_X	= Edge energy.
$\chi(k)$	= Oscillatory part of the core edge intensity.
N_j	= Number of atoms in the jth coordination shell.
R_j	= Radius of jth coordination shell.
$f_j(k)$	= Backscattering amplitude function.
A(k)	= Factor including range of ejected electron and temperature effects.
$\varnothing_j(k)$	= Total phase shift for ejected electron.

DESCRIPTION OF INELASTIC SCATTERING PROCESSES

Kinematics

When a fast electron is scattered inelastically it transfers energy E and momentum $\underline{q}$ to the sample. The incident electron can normally be considered to be in a plane wave state exp $(i\,\underline{k}\cdot\underline{r})$ where $\underline{r}$ is its position vector and $\underline{k}$ is its wave vector. The initial energy can be written as,

$$E_0 = \frac{\hbar^2 k^2}{2m} \qquad 1$$

and the final energy as,

$$E_0 - E = \frac{\hbar^2 k'^2}{2m} \qquad 2$$

where $\underline{k}'$ is the scattered wave vector. The momentum transfer to the sample is

$$\hbar \underline{q} = \hbar (\underline{k} - \underline{k}') \qquad 3$$

Since in practice we measure the scattering angle Θ it is useful to relate this to the momentum transfer. We consider the component parallel and perpendicular to the incident beam. Then for small Θ we have

$$q^2 = q_\perp^2 + q_{/\!/}^2 = k^2(\Theta^2 + \Theta_E{}^2) \qquad 4$$

where $\Theta_E = E/2E_0$ is the characteristic scattering angle. The quantity $q_{/\!/} = k\Theta_E$ is therefore also the minimum momentum transfer that can be given to the sample. To describe the inelastic scattering processes we require the differential cross section with respect to E and $\underline{q}$. This can be obtained by using the Born approximation which assumes that the energy loss and momentum transfer are small compared with the energy and momentum of the incident beam (weak interaction). The cross section is written as (Bethe, 1930),

$$\frac{d^2\sigma}{dE\, d\Omega} = \frac{4}{a_0{}^2 q^4} S(\underline{q}, E) \qquad 5$$

where $d\Omega$ is an element of solid angle and $S(\underline{q},E)$ is a dynamical form factor for inelastic scattering, a property of the unperturbed sample. The factor $4/(a_0{}^2q^4)$ is essentially the Rutherford cross section for scattering from a point charge. The form factor is normally expressed in two different ways, one appropriate for valence excitations and the other for core excitations. In general we note that $S(\underline{q},E)$ involves the square of matrix elements for transitions from an initial to a final state.

Valence electron excitations

Excitation of valence electrons in a solid is in general a many-electron problem since the Coulomb force which interacts between them is of long range. Wavefunctions describing the initial and final states are so complicated that certain simplifications must be made. We use the concept of screening (Pines, 1964) where each electron carries with it a region of positive charge due to the Coulomb repulsion of other electrons. The net interaction is then short range. Each electron therefore appears to be neutral from a distance. If a fast electron enters the system (applied field) the neighboring electrons move to screen it but overshoot and oscillate at a frequency corresponding to the classical plasma frequency,

$$\omega_p = \left(\frac{4\pi n e^2}{m}\right)^{1/2} \qquad 6$$

where n is the density of conduction electrons.

In simple terms this is the origin of the plasmon in a solid. To understand the problem further we need information about the space and time dependence of the screening cloud surrounding each electron. This is related to the polarizability of the system of electrons and to the complex dielectric constant $\epsilon(\underline{r},t)$ or its Fourier transform $\epsilon(\underline{q},E)$. It is therefore possible to write the form factor $S(\underline{q},E)$ in terms of $\epsilon(\underline{q},E)$ which gives a description of the scattering in terms of a macroscopic quantity obtainable from other means.

It has been shown (Pines, 1964) that

$$S(\underline{q},E) = \frac{q^2}{4\pi^2 ne^2} \operatorname{Im}\left(-\frac{1}{\epsilon(\underline{q},E)}\right) \qquad 7$$

Equations 5 and 7 give us the general momentum-transfer dependence of the spectrum which falls off as $1/q^2$. The angular distribution is therefore a Lorentzian of width Θ_E, modified by whatever angular dependence there is in $\epsilon(q,E)$. The dielectric constant can be written in terms of a real part ϵ_1, and an imaginary part ϵ_2. Therefore we have,

$$\operatorname{Im}\left(-\frac{1}{\epsilon}\right) = \frac{\epsilon_2}{\epsilon_1{}^2 + \epsilon_2{}^2} \qquad 8$$

Here ϵ_1 describes refraction of the fast electron and ϵ_2 describes absorption of energy. Optical absorption spectra are described by ϵ_2 when $q \rightarrow 0$. The different form of the energy loss spectrum comes about because the fast electron gives rise to a longitudinal field producing density changes of the valence electrons in the q-direction. Photons only produce a transverse field which does not affect their density. The condition for plasmon excitations to occur is that ϵ_2 becomes small and $\epsilon_1 \rightarrow 0$. Single-electron (interband or intraband) transitions occur as maxima in ϵ_2. At high energy losses $\epsilon_1 \rightarrow 1$ and $\epsilon_2 \ll 1$. In this energy region

$$\operatorname{Im}\left(-\frac{1}{\epsilon}\right) \rightarrow \epsilon_2$$

and the energy loss spectrum has the same form as the optical absorption spectrum. In general the real and imaginary parts of ϵ can be derived from

$$\operatorname{Im}\left(-\frac{1}{\epsilon}\right)$$

by the Kramers-Kronig relations, so the energy loss spectrum can be related to the optical absorption coefficient for all energies (Daniels et al., 1970). An important advantage of electron energy loss spectroscopy is the possibility of studying the q-dependence of different excitation processes. For example bulk plasmons display a dispersion relation that is quadratic in q, and this can help to identify the excitation process (Batson et al., 1976). The q-dependence of interband transitions is different and this can provide information about non-vertical excitations (Chen and Silcox, 1977) or

about how the energy bands in a solid bend across the Brillouin zone. In such experiments the transition probability depends on a joint density-of-states between the unoccupied and occupied bands and the interpretation can be complicated. We shall see below that the core edges essentially only involve a single density-of-states.

Because the total mean free path for valence electron excitation is only a few tens of nm at 100 keV beam energy, plural inelastic scattering is inevitable. It has proved very important to derive the single-scattering intensity before a detailed analysis is possible (Batson, 1976).

Core Excitations

Since the inner shell levels of an atom are highly localized, the form factor or cross section for core ionization can be considered as basically an atomic quantity, with the effects of the solid added as a refinement afterwards. The probability for core excitation may be expressed in terms of a one-electron transition matrix element between an initial core state $|i\rangle$ and a final unoccupied state $|f\rangle$. Within the Born approximation the form factor is given by (Bethe, 1930),

$$S(\underline{q},E) = |\langle f|\exp(i\underline{q}\cdot\underline{r})|i\rangle|^2 \qquad 9$$

where the operator $\exp(i\underline{q}\cdot\underline{r})$ arises from the interaction between the bound electron and the fast electron. The core spectrum consists of characteristic edges at energies corresponding to the binding energies of the initial states $|i\rangle$ which are 1s, 2s, 2p, 3s, 3p, 3d etc. atomic levels; final states $|f\rangle$ mostly lie in the continuum and are taken to be normalized per unit energy range. It is useful to express the cross section in terms of a generalized oscillator strength,

$$\frac{df}{dE}(\underline{q},E),$$

which is similar to the optical oscillator strength in the limit $q \rightarrow 0$. This is given by (Inokuti, 1971),

$$\frac{df}{dE}(\underline{q},E) = \frac{2mE}{\hbar^2 q^2}|\langle f|\exp(i\underline{q}\cdot\underline{r})|i\rangle|^2 \qquad 10$$

From Equations 4 , 5 , 9 and 10 we can write the differential cross section in terms of the measured quantities E and Θ.

$$\frac{d^2\sigma}{dE\,d\Omega} = \frac{e^4}{E_0 E}\left(\frac{1}{\Theta^2+\Theta_E^2}\right)\frac{df}{dE}(\underline{q}E) \qquad 11$$

To make this formula relativistically correct the energy E_0 is replaced by

$$\frac{mv^2}{2}$$

where $\underline{v}$ is the electron velocity. Equation 11 demonstrates that the angular distribution for core excitation is dominated by the Lorentzian factor as for the valence excitations. However as discussed by Inokuti (1971) the generalized oscillator strength can peak at non-zero Θ especially at energies far above an edge threshold.

Total cross sections can be obtained by integrating

$$\frac{d^2\sigma}{dE\,d\Omega}$$

over an appropriate range of E and Θ. The cross sections are important for quantitative analysis of energy loss spectra. Computations of generalized oscillator strengths have been carried out by several authors by calculating the atomic bound and continuum wave functions (Inokuti, 1971; Manson, 1972; Leapman et al., 1980). In order to see the relation between the energy loss spectrum and the x-ray absorption spectrum it is convenient to expand the operator in the matrix element in Equation 9 as,

$$\exp(i\underline{q}\cdot\underline{r}) = 1 + iq(\hat{\epsilon}_q\cdot\underline{r}) - \frac{q^2}{2}(\hat{\epsilon}_q\cdot\underline{r})^2 + \ldots \qquad 12$$

where $\hat{\epsilon}_q$ is a unit vector in the direction of $\underline{q}$. The first term vanishes since $|i\rangle$ and $|f\rangle$ are othogonal. The second term has exactly the same form as the dipole matrix element for absorption of x-rays where $\hat{\epsilon}_q$ is replaced by the polarization vector of the electric field. This dipole term gives rise to transitions involving a change in angular momentum quantum number $\Delta\ell = \pm 1$. It is normally by far the most important and is heavily favored by the

$$\frac{1}{q^2}$$

factor in the cross section. Thus transitions from the K shell (ls level) are mainly to states of p-symmetry, and transitions from the L_{23} shell (2 p level) are to states of d-or s-symmetry. At larger scattering angles

$$q \sim \frac{1}{r_c},$$

where r_c is the core wavefunction radius, non-dipole transitions may be observed, so that the dipole selection rules do not apply. Such excitations can show a different q-dependence. The third term in Equation 12 gives rise for example to quadrupole (or monopole) transitions that have an intensity independent of q (Grunes and Leapman, 1980).

Finally we mention here briefly the effect of the solid on the core edges, as this will be discussed in more detail later on. We can write the intensity in the spectrum as the product of two factors, a slowly varying atomic matrix element P(E) and a density-of-states N(E) of appropriate symmetry,

$$I(E) = N(E)\cdot P(E) \qquad 13$$

The initial core level is considered in this simple approach to be a δ-function in energy so the spectral shape is related only to the density of unoccupied conduction states.

SOME ASPECTS OF INSTRUMENTATION

Electron energy loss spectroscopy (EELS) can be carried out both in the dedicated scanning transmission electron microscope (STEM) and in the conventional transmission electron microscope (CTEM) with a STEM attachment. Normally the STEM is equipped with a field emission gun which produces a small source size and can therefore focus electrons

into a probe diameter as low as 3 to 5 Å with a current in excess of 1 nA. This type of source is essential if high spatial resolution is required. Moreover the energy spread of the cold field emission source is only about 0.2 eV so that high energy resolution in the spectrum is also possible (Isaacson, 1972; Crewe et al., 1971; Brown, 1981). The CTEM-STEM normally operates with a heated tungsten filament source which can only produce a probe diameter of about 100 Å with a current of 1 nA, but unlike the dedicated STEM, it does not require an ultrahigh vacuum system. The energy spread of the source is about 1 eV so it is not possible to record spectra at higher resolution than this, unless a monochromator is used. A third type of source, lanthanum hexaboride, can yield a smaller probe size of around 30 Å but the energy spread is still 1 eV. Typically both types of scanning instruments operate at about 100 keV beam voltage. However the CTEM has also been designed for higher voltages (~ 1 MeV) and this has some important advantages (Jouffrey and Sevely, 1976; Jouffrey et al., 1978). As the incident beam energy increases the inelastic cross sections fall and plural scattering becomes less. This is one of the major limitations in EELS. Also as the beam energy increases the scattering angles decrease and collection efficiency improves for high energy losses (several thousand eV).

The CTEM-STEM has the convenience of intermediate and projector lenses after the sample to help couple the electrons into the spectrometer. In the dedicated STEM these lenses have to be added specially. The CTEM also has the flexibility of allowing us to record spectra from extended regions of the sample by operation in the diffraction mode (Wittry, 1969; Curtis and Silcox, 1971; Krivanek, 1979). The incident beam can then be highly collimated, making possible studies at high angular or momentum resolution. In the STEM the probe convergence angle on the sample is usually several mrads so the momentum resolution is limited. It is therefore evident that both instruments have certain advantages for EELS.

Let us now consider a CTEM-STEM coupled with an electron spectrometer of the magnetic sector type. This arrangement is being widely used (Joy and Maher, 1978a; Johnson, 1979; Krivanek, 1979; Egerton, 1980a; Shuman, 1980) and a schematic diagram giving the important features of a complete system is shown in Fig. 1. Electrons from a point crossover of the intermediate lens enter the spectrometer which refocusses them in another plane. In passing through the spectrometer, in this case a 90° sector, the electrons are also dispersed in energy in a line parallel to the pole-pieces. If the radius of curvature of the magnetic sector is R the dispersion is given by,

$$D \sim \frac{2R}{E_0} \qquad 14$$

D typically takes a value of a few μm per eV and to obtain a good energy resolution a narrow slit must be placed in the dispersion plane. The spectrometer pole-pieces are inclined to the normal so that fringing fields are produced which focus the electrons in a perpendicular direction. In fact the performance depends on careful design of the spectrometer and appropriate coupling to the microscope. For many systems the energy resolution ΔE is limited by second-order aberrations which depend on the square of the acceptance angle γ,

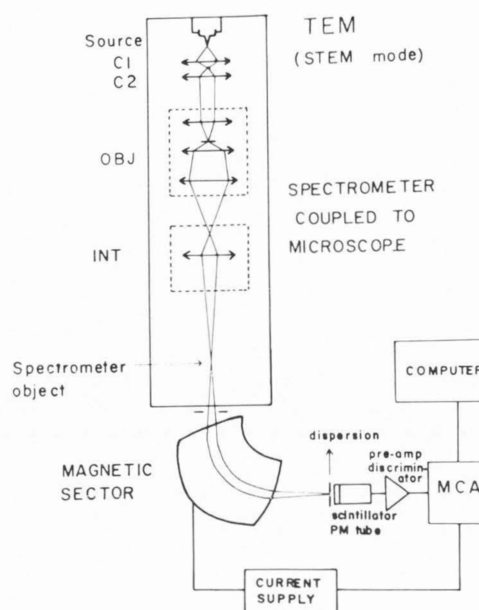

Fig. 1. Schematic diagram showing some of the main features of an electron energy loss system coupled to a CTEM with a STEM attachment. C1 and C2 are the condenser lenses which together with the pre-field of the objective (OBJ) form a probe on the sample. The probe can be scanned to produce an image or stopped on a particular area of the sample to collect a spectrum. The post-field of the objective and the intermediate (INT) couple the transmitted electrons into the spectrometer.

$$\Delta E = \frac{C\gamma^2}{D} \qquad 15$$

where C is the second order aberration coefficient.

In order to obtain a good resolution it often turns out that γ is much less than the optimum collection angle $\propto$ of electrons from the sample. Hence there is a great advantage in using the intermediate lens (Fig. 1) to demagnify the angles from the sample into the spectrometer as is discussed by Johnson (1980) and Egerton (1980b). If M is the image magnification of the lenses after the sample,

$$\gamma = \frac{\propto}{M} \qquad 16$$

Second order aberrations can be corrected by carefully rounding the polepieces or by using sextupole lenses (Shuman, 1980). Nevertheless some aberrations remain so efficient coupling is still desirable, especially since large collection angles (~ 50 mrads) are often required. To record the spectrum we can ramp the dispersed electrons across the analyzing slit; this can be achieved by varying the magnetic sector current or by using coils or electrostatic deflection

plates after the spectrometer. The electrons strike a scintillator and the light produced is amplified by photomultiplier. The resulting electrical pulse is preamplified, discriminated and passed into a multichannel analyzer for display. It is desirable to interface the multichannel analyzer to a larger computer for storage and data processing.

Such a system is capable of pulse counting single electrons at a rate in excess of 10^7Hz. However the spectrum is recorded serially one channel at a time. Recently attempts have been made to develop electronic parallel recording devices which can count many channels simultaneously, thereby increasing the collection efficiency. Previously the only parallel detection method available has been photographic film, which has been very useful but inconvenient. The most promising electronic parallel detection systems convert the dispersed electrons into light which can then be magnified and focussed on to the recording device. Direct exposure of the device to fast electrons can cause problems due to radiation damage. Shuman (1981) has developed a fiber-optic coupling to a silicon intensified target (SIT) vidicon tube. Optical lenses are used to image the spectrum from a phosphor onto the SIT photocathode. Also a magnetic lens is placed after the spectrometer to increase the energy dispersion. An energy resolution of a few eV has been demonstrated. Other parallel detection systems have been developed by Johnson et al. (1981) and Egerton (1981a) who have used image intensifiers and linear photodiode arrays.

Finally, we should note that although we have only mentioned the magnetic sector spectrometer, many other types exist which use combinations of electrostatic and magnetic fields. Some of these are capable of very high energy resolution, especially those which retard the electron beam before the dispersion occurs (Schnatterly, 1979; Ritsko and Mele, 1980). We do not have space either to discuss another type of instrument, the energy filtering microscope, which is capable of forming energy selected images in the TEM mode (Castaing and Henry, 1962; Rossouw et al., 1977; Zanchi et al., 1977).

INFORMATION FROM LOW LOSSES

We have already given a brief description of the valence excitations; let us now examine some spectra to show what sort of information can be extracted.

Figure 2 shows data from a beryllium alloy containing precipitates of beryllium oxide a few hundred Å in diameter. The low loss spectrum from one such precipitate of BeO is compared with the matrix. The width of the zero-loss peak indicates that the energy resolution is 2eV. It is noted that the zero-loss peak also contains electrons which are scattered elastically inside the collection aperture as well as quasi-elastically (phonon) scattered electrons which suffer energy losses less than about 0.1 eV. A significant shift between the metal and oxide plasmon peaks is evident, their energies being ~ 17 eV and 25 eV respectively. The plasmon is relatively narrow in the metal which is free-electron-like whereas the oxide is more complicated and the peak at 25 eV is only partially collective in nature, being broadened by single-electron excitations. Qualitatively the increased energy of the plasmon-type peak in the oxide can be explained by the greater number of valence electrons in the solid. A difference in spectral shape is also visible at lower energies. In the metal there is evidence for intraband transitions at a few eV energy, as expected from the existence of a partially filled conduction band. Beryllium oxide is a strong insulator however, and this explains why the intensity falls to zero and only begins to rise again at about 7 eV, corresponding to the band gap.

Figure 2 also demonstrates the presence of plural inelastic scattering which produces additional peaks at twice the plasmon energy in both Be and BeO. Plural scattering is governed by a Poisson distribution, where the probability of single scattering is proportional to the thickness t, double scattering goes as t^2, etc. The measured intensity in the spectrum I(E) can be written (Batson, 1976) in terms of a series of convolutions,

$$I(E) = \exp(-t/\lambda_T) I_0(E) * [\delta(E) + tQ(E) + \left(\frac{t^2}{2!}\right) Q(E) * Q(E) + \ldots.] \quad 17$$

where Q(E) is the single scattering distribution, $I_0(E)$ is the instrumental resolution function, $\delta(E)$ represents the unscattered beam, and λ_T is the total mean free path for inelastic scattering. In general this equation should also be expressed in terms of $\underline{q}$ or Θ, but for simplicity we have omitted the angular dependence here. A quantitative understanding of the spectrum can in general only be achieved by deriving Q(E) or Q(E, Θ). Several authors have demonstrated that the single scattering distribution can be retrieved from the measured spectrum (Johnson and Spence, 1974; Batson, 1976). Their method involves taking a Fourier transform of Equation 17 , thus leaving a simple exponential series which can be inverted by means of the complex logarithm function.

Equation 17 gives a very simple expression for the sample thickness in terms of λ_T.

$$t = \lambda_T \ell n \left(\frac{I_T}{I_Z}\right) \quad 18$$

where I_T and I_Z are respectively the areas under the entire spectrum and the zero loss peak. This can provide the basis for an accurate thickness determination if λ_T is known.

We now consider an example of how more detailed information can be obtained from the valence excitations. Fig. 3 shows the low loss spectrum recorded by Ritsko and Mele (1980) from a sample of graphite intercalated with ferric chloride to give the stage-1 compound. For comparison the spectrum from pure graphite is also displayed in Fig. 3. The data was collected using a specially designed electrostatic spectrometer system capable of 0.1 eV energy resolution. These authors interpret the spectra as follows. Since graphite is a semi-metal with a completely filled valence band and an empty conduction band, removal of charge by the intercalent results in a partial emptying of the valence band. New intraband excitations are then possible and these are evident as a strong peak at ~ 1 eV. In fact from its dispersion as a function of q it is deduced that the peak is an intraband plasmon. A more detailed analysis of the excitation yields an accurate measurement of the charge transfer (Ritsko and Mele, 1980).

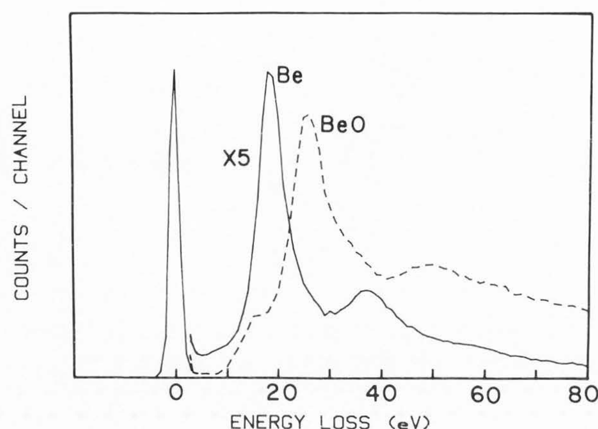

Fig. 2. Low loss spectra from a 200 Å diameter beryllium oxide precipitate in a beryllium alloy compared with the spectrum from the matrix.

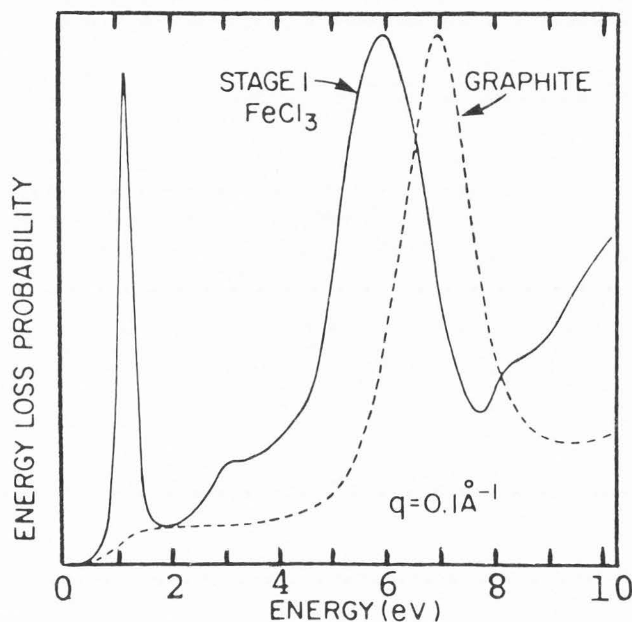

Fig. 3. Energy loss spectra recorded by Ritsko and Mele (1980) from $FeCl_3$ intercalated stage-1 graphite and pure graphite. An intraband transition at about 1 eV is evident in the intercalated compound. The peak at 7 eV in graphite, shifted to 6 eV in the intercalated compound, is the π interband plasmon. The data was recorded with a momentum transfer, $q = 0.1$ Å^{-1}.

The peak at 7 eV in graphite is a π plasmon excitation. It is observed at lower energy in the intercalated compound because the graphite planes are further apart and the electron density is lower.

We are not able to discuss the low loss spectra in more detail here but list some other areas where important data have been obtained. Studies have been made for example on metals (Batson et al., 1976),on semiconductors (Chen et al., 1975) and on surface excitations in anisotropic materials (Chen and Silcox, 1975; Ray, 1981).

MICROANALYSIS

Quantitation

The advantage of using EELS for the detection of light elements has been well demonstrated. Low fluorescence yield and poor collection efficiency make the conventional x-ray microprobe technique insensitive for low Z. In contrast the efficiency for detecting inner shell ionization events by EELS is high and the K and L shell cross sections for the lighter elements are particularly favorable. It has also become apparent that heavier elements can be detected by their M and N edges, but these edges are somewhat more complicated in shape (Colliex and Trebbia, 1978) and are more difficult to quantitate. The basic groundwork for quantitation has been given by Isaacson and Johnson (1975). The measured signal (counts) per eV of the spectrum

$$\frac{dS_X}{dE}$$

for a core excitation X is,

$$\frac{dS_x}{dE} = \left(\frac{J}{e}\right) \tau \frac{d\sigma_X}{dE}(\alpha, E)\, N_X \qquad 19$$

where J is the incident probe current, τ is the integrating time, N_X is the number of atoms X per unit area of the same and

$$\frac{d\sigma_X}{dE}(\alpha, E)$$

is the differential cross section per atom integrated over a collection semi-angle α. Equation 19 can be rearranged to give the absolute number of atoms per unit area in terms of the intensities in the core edge and in the low loss part of the spectrum. The quantity, $I = J\tau/e$, is simply equal to the total number of counts in the spectrum if collection is over all angles. In practice only a limited collection angle α and a limited energy window Δ above the edge threshold can be used. Egerton and Whelan (1974a) have given an expression for N_X in terms of the measured counts in the core edge $S_X(\alpha, \Delta)$ and the measured counts in the low loss spectrum $I(\alpha, \Delta)$, both quantities being obtained for an appropriate α and Δ,

$$N_X = \frac{S_X(\alpha, \Delta)}{I(\alpha, \Delta)\, \sigma_X(\alpha, \Delta)} \qquad 20$$

where $\sigma_X(\alpha, \Delta)$ is the partial integrated cross section. This formula takes some account of mixed scattering (plural inelastic and elastic-inelastic) by assuming that the low loss spectrum is affected in the same way as the core edge. Although only approximate it has been found experimentally to be satisfactory for many applications (Joy et al., 1979; Joy and Maher, 1981). Often, however, it is the ratio of two or more elements that is important and this is simply given by the ratio of their integrated edge intensities divided by the ratios of the corresponding partial cross sections (Leapman, 1979).

The intensity under the core edge is found by extrapolating the background intensity arising from the tails of other core

losses. It has been shown (Egerton and Whelan 1974a; Egerton, 1975) that the background intensity

$$\frac{dB}{dE}$$

follows closely an inverse power law,

$$\frac{dB}{dE} = AE^{-r} \qquad 21$$

where A and r are constants with r typically taking a value between 3 and 4 depending on the collection angle. In order to obtain quantitative results we must obtain values for the partial cross sections $\sigma_X(\alpha, \Delta)$.

Cross Sections

Several approaches have been taken to estimate the partial cross sections. The most straightforward method which was only intended to be approximate has been described by Isaacson and Johnson (1975). The partial cross section is separated into three factors, the angular collection efficiency $\eta(\alpha)$, the energy window efficiency $\eta(\Delta)$ and the total cross section for core level ionization σ_T.

$$\sigma_X(\alpha, \Delta) = \eta(\alpha)\eta(\Delta)\sigma_T \qquad 22$$

The fraction of electrons scattered inside collection angle α, $\eta(\alpha)$, may be calculated from the Lorentzian distribution in Equation 11. It is assumed that there is no q-dependence of the oscillator strength but that

$$\frac{df}{dE}$$

drops to zero at a cut-off angle, $\Theta_{max} = \sqrt{2\Theta_E}$, corresponding to the "classical" scattering angle for free-electrons. The factor $\eta(\Delta)$ may be estimated from Equation 21 assuming that the spectrum above the edge follows an inverse power law similar to the background preceding the edge, a reasonable approximation far above threshold. Isaacson (1980) has refined the estimation of $\eta(\Delta)$ by allowing for variations in the exponent r in the inverse power law as a function of collection angle. The total cross section may be obtained from calculations and experimental data discussed for example by Powell (1976).

Egerton (1979) has used another method which depends on the hydrogenic wavefunction approximation. The generalized oscillator strength for the hydrogen atom can be expressed in an analytical form. Thus the partial cross sections can be found by integration over the appropriate limits of Θ and E. Measurements have shown that the hydrogenic cross sections for K edges are accurate to within ± 5 or 10% (Joy and Maher, 1981). Recently Egerton (1981b) has adapted the hydrogenic method to apply to L edges by including an atomic screening constant. Results agree with more complete atomic calculations.

The partial cross sections can be found directly from the generalized oscillator strength (Inokuti, 1971). The initial and final state wavefunction in Equation 10 can be calculated from an atomic Hartree-Slater program (Manson, 1972; Leapman et al. 1980; Rez and Leapman, 1981). The initial

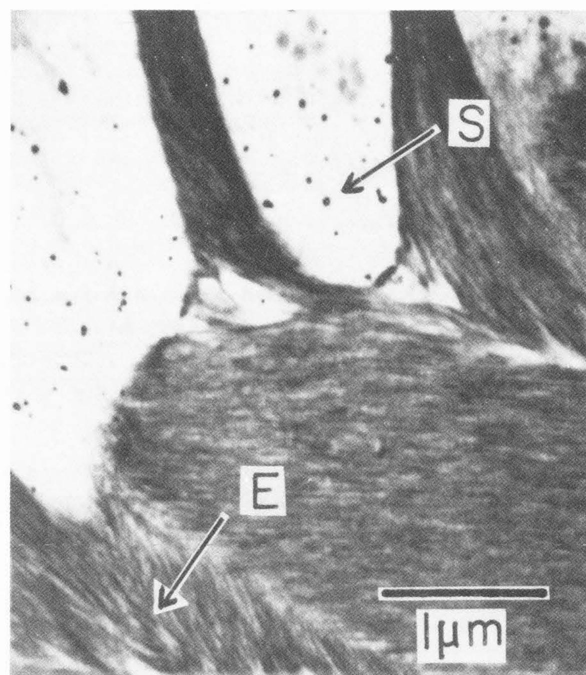

Fig. 4. STEM image from a section of embedded tooth showing an area of immature enamel (E) containing crystallites of hydroxyapatite in an organic matrix. The light areas in the top left are ameloblasts (enamel forming cells). These contain secretory granules (S) with deposits of calcium pyroantimonate.

state is taken as a one-electron wavefunction solved with a self-consistent potential and with averaged exchange, and the final continuum states are computed by solving a Schrödinger equation with the same potential. An advantage of this approach is that it can be used for L, M and N edges as well as K edges. It also predicts a number of shape effects. For example the M_{45} edges (3d excitations) for the elements Z=40 to 50 are characterized by a delayed onset occurring about 20 or 30 eV above threshold. This effect can be attributed to a "centrifugal barrier" in the atomic potential for the final state with f-symmetry so the overlap with the initial state is reduced until the barrier is surmounted (Manson, 1972; Leapman et al., 1980). In such cases identification and quantitation of the element can be frustrated. The atomic calculations also predict variations in edge shape across the periodic table. Thus the L_{23} edges (2p excitation) in Al, Si, P, S and Cl display a broad maximum about 20 eV above threshold, while K, Ca and the first transition period elements exhibit intense peaks just above threshold. It is not yet established how accurately such cross section calculations can be made for M and N excitations and this is an area for future work.

An Analytical Example

To demonstrate these quantitation procedures and some of the problems that can occur we consider one example, the analysis of a biological sample.

Figure 4 shows a STEM bright-field image from a thin

embedded section of tooth containing ameloblast cells and regions of immature enamel. The sample had been previously fixed with potassium pyroantimonate to precipitate calcium inside the cells (Leapman, 1982). Figure 5 shows the spectrum recorded at 100 keV beam energy with a 10 mrad acceptance angle from a dense enamel crystallite in the immature enamel surrounding the ameloblasts. The P L_{23} (132 eV), C K (285 eV), Ca L_{23} (346 eV) and O K (532 eV) excitations are clearly visible and we notice that the edge shapes for all these elements are different. Also shown in Fig. 5 are the subtracted edges for P, Ca and O. The atomic ratio of P:Ca is obtained from the partial cross sections as calculated from the Hartree-Slater atomic calculation with $\alpha = 100$ mrads and $\Delta = 100$ eV. A result of P:Ca = 0.63:1 is obtained. This is very close to the expected result for hydroxyapatite from which enamel is composed (P:Ca = 0.60:1). The estimated O:P atomic ratios is 9.5:1 indicating that about half the oxygen in this area of the specimen came from the embedding material or organic matrix, the presence of which is also indicated by the carbon K edge.

Of special interest in this sample is the composition of the dense deposits in the ameloblasts (light areas in Fig. 4). The spectrum from one such deposit about 20 nm in diameter is shown in Fig. 6. The calcium L_{23} edge is observed as well as the oxygen K edge at ~ 532 eV. However instead of phosphorus a second broad maximum is visible above the oxygen K edge. This can be attributed to the antimony M_{45} edge, expected from the treatment of the sample with pyroantimonate. The Sb M_5 binding energy is almost identical to that of the oxygen K edge but these elements can in fact be distinguished by their different edge shapes. As yet there is no method for obtaining quantitative results from such overlapping edges. We note that in this analysis Ca could not be detected by x-ray emission because of overlap of the Ca K_α line with Sb L_α line. This serves as a good example of the complementarity of EELS and x-ray microanalysis.

Correction for plural scattering

The shape of the energy loss spectrum can be strongly influenced by plural inelastic scattering as was discussed earlier in the context of the low loss spectrum. For accurate quantitative results it is useful to derive the single scattering distribution and in some cases this may be necessary even to identify an element. The very large dynamic range of the core excitations which generally varies over four or five orders of magnitude from 0 to 2000 eV makes it difficult to use Equation 17 . For core edges the problem may be simplified by considering the measured core edge intensity I(E) to be the convolution of the single scattering core loss distribution with the observed low loss spectrum L(E) provided the collection angle α is large so that angular effects are neglibible. The single scattering distribution Q(E) can then be derived by a deconvolution procedure (Egerton and Whelan, 1974b; Leapman and Swyt, 1981). It is assumed that the pre-edge background can be subtracted off first using the inverse power law. We can now write,

$$I(E) = L(E) * Q(E) \qquad 23$$

The deconvolution may be performed by using Fourier transforms but in practice it is necessary to reconvolute by the normalized instrumental resolution function $I_0(E)$ in order to truncate the high frequency coefficients (Johnson and Spence, 1974). Then denoting Fourier coefficients by lower case and the inverse Fourier transform by F^{-1} we have an expression for the broadened single scattering distribution

$$Q'(E) = F^{-1}\left[\frac{i(e)\, i_0(e)}{\ell(e)}\right] \qquad 24$$

Figure 7 shows the measured and deconvoluted intensity for the boron K edge in a sample of hexagonal boron nitride with thickness $t = 1.0\lambda_T$. It is evident that the intensity 30 eV or so above threshold is modified substantially. The fine structure near the core edge is not affected strongly since the energy from threshold is much less than the plasmon energy (~ 25 eV). Measurements seem to indicate that the effect of thickness on quantitation is not as great as might be expected since the edges in the spectrum are altered in approximately the same way by plural scattering. For an accuracy of $\sim 10\%$ or better the single scattering distribution should probably be derived. However often other errors limit the analysis. For

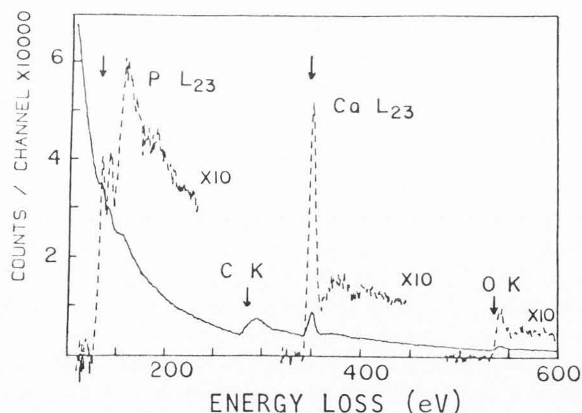

Fig. 5. Energy loss spectrum from enamel crystallite showing P L_{23}, C K, Ca L_{23} and O K edges. The background is subtracted for P, Ca and O.

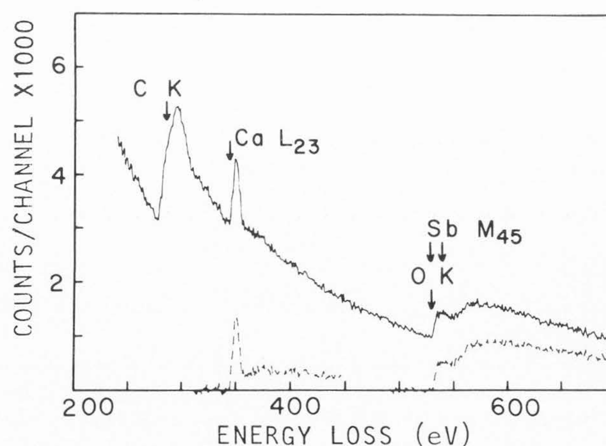

Fig. 6. Energy loss spectrum from dense deposit in secretory granule showing C K, Ca L_{23}, O K and Sb M_{45} edges.

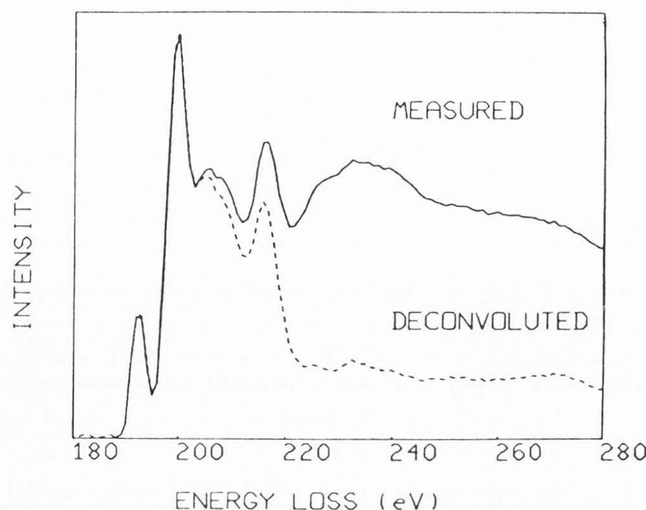

Fig. 7. Measured and deconvoluted boron K edge from a sample of boron nitride with thickness $t = 1.0\lambda_T$.

example it is especially important to know the collection angle α since the partial cross sections depend strongly on this parameter. If this angle is defined by the objective aperture of the microscope, α can be calibrated from a known diffraction pattern.

Optimization, detection limits and resolution

As was originally proposed by Isaacson and Johnson (1975), Equation 19 can be used to estimate the detection limits for microanalysis. These limits of course depend on the type of probe forming system that is used. A field emission source is capable of forming a beam of diameter 3 to 5 Å so that the minimum detectable mass is very much smaller than that obtainable from a heated tungsten filament source which is only capable of forming a 100 Å probe. When however we are interested in detecting a low concentration of an element distributed uniformly over a larger area, it is the minimum detectable atomic fraction that is important and not the probe size.

If the signal in a channel of width δE is δS and the background is δB then we require the signal to be about three times the statistical fluctuation,

$$\delta S \gtrsim 3\sqrt{\delta S + \delta B} \qquad 25$$

Apart from the type of source other instrumental parameters affect the detection limits such as the collection angle and energy window above threshold (Joy and Maher, 1978b). Usually it is advantageous to use as large a collection angle as possible but sometimes the signal/noise is a maximum at some intermediate value. This is because the background under an edge has a different angular distribution from that of the signal.

From Equations 19 and 25 we can obtain an expression for the minimum atomic fraction of an element X in a matrix B that contributes to the background (Joy and Maher, 1980). We assume that the number of atoms per unit area $N_X \ll N_B$ so,

$$\left(\frac{N_X}{N_B}\right)_{min} \cong \frac{3\sqrt{\frac{d\sigma_B}{dE}}}{\frac{d\sigma_X}{dE}\sqrt{J\,\tau\,\delta E N_B}} \qquad 26$$

where $\frac{d\sigma_B}{dE}$ and $\frac{d\sigma_X}{dE}$ are the differential cross sections of the background and the signal respectively for some collection angle α.

As an example let us estimate the minimum atomic fraction of calcium atoms in a carbon matrix. We assume the following sample and instrumental parameters:

E_0 = 100 keV
α = 10 mrads
J = 1 nA
τ = 1 sec/channel
δE = 2eV channel width
$\frac{d\sigma_B}{dE} = 5\times10^{-27}\,m^2eV^{-1}$ (C K cross section at Ca L_{23} edge)
$\frac{d\sigma_X}{dE} = 5\times10^{-26}\,m^2eV^{-1}$ (Ca L_{23} cross section at threshold)
t = 200 Å
density of carbon = 2×10^3 Kg m^{-3}

The differential cross sections were estimated from atomic calculations (Leapman et al. 1980). Equation 26 yields a minimum atomic fraction of 8×10^{-4}. The minimum detectable atom fraction in general depends strongly on the cross sections and detection of calcium in carbon is favorable because of the sharp peak at threshold (Fig. 5). Typically with the same instrumental parameters $(N_X/N_B)_{min}$ ranges from 10^{-2} to 5×10^{-4} for other elements. EELS is clearly not a trace microanalytical technique but fairly small concentrations can be detected. The important point is that with a probe diameter of only 3 to 5 Å, the minimum detectable number of atoms is very low, probably between 1 and 10 atoms.

Finally we should mention that the localization of such small amounts of matter by electron energy loss spectroscopy is only possible if the scattering interactions between the atoms and the incident beam are themselves localized. As has been discussed by Howie (1981), the impact parameter b in the scattering event is related to the momentum transfer by the uncertainty principle. We can roughly write $b = q^{-1}$. For the low energy valence losses b is around 100 Å so a high degree of localization is not possible. For energy losses in the range 200 to 1000 eV, the impact parameter is typically a few Å and this seems to represent the resolution limit of core loss spectroscopy. This turns out to be comparable with the near atomic sensitivity predicted by the statistics for optimized instrumentation. Such estimates of course ignore the susceptibility of the sample to beam damage under the very high current densities required. In organic or biological specimens this will always be the chief limitation (Isaacson et al., 1978).

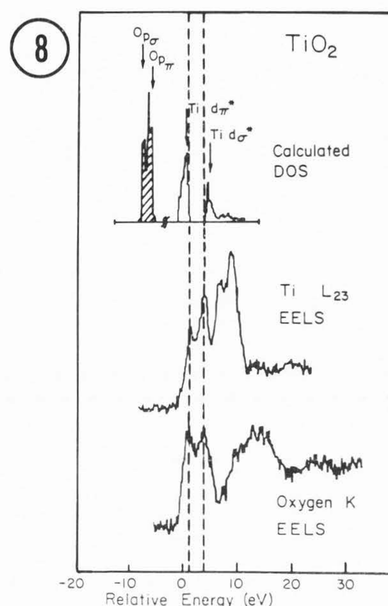

Fig. 8. Core edge fine structure in TiO_2 showing the Ti L_{23} and O K edges. Comparison is made with the calculated density-of-states (Grunes et al., 1982). The shaded area corresponds to filled states originating from oxygen p(σ) and p(π) orbitals. Unfilled states originate from titanium d(σ^*) and d (π^*) orbitals. Vertical dashed lines show the correspondence between the observed double peak at the core edges and the double maximum in the calculated density of states.

CHEMICAL BONDING AND ELECTRONIC STRUCTURE

Near-edge fine structure

In the most simple model, fine structure in the region of the core edges may be attributed to features associated with unoccupied conduction states (Colliex and Jouffrey, 1972; Egerton and Whelan, 1974c) or in the case of organic solids with the excited molecular levels (Isaacson, 1972). However, it should be remembered that atomic effects can also strongly influence the shape of core edges especially for M and N excitations in heavier elements (Trebbia and Colliex, 1973; Brousseau-Lahaye et al., 1975; Colliex and Trebbia, 1978). We find that the subject is so complex that a complete interpretation of the fine structure is not available (Brown, 1974). Nevertheless some important and detailed information can be obtained. We have already seen that the dipole selection rules apply for small momentum transfers so that transitions involve a change in angular momentum $\Delta\ell = \pm 1$. This fact can be put to use and to some extent it is possible to choose the symmetry of the final states by selecting a particular edge.

To demonstrate the type of results that may be obtained we consider the core edges in titanium dioxide. Figure 8 shows the region near the oxygen K edge (530 eV) and the titanium L_{23} edge (459 eV) from a 15 nm film of evaporated metal which had been oxidized in air (Grunes et al., 1982). The spectrum was recorded using a retarding field Wien filter spectrometer combined with a transmission electron microscope capable of ~ 1 eV resolution in this energy range (Curtis and Silcox, 1971). Both the O K edge and the Ti L_3 edge display a double maximum at threshold with a peak separation of ~ 2.5 eV. Some understanding for the origin of these peaks is given by a simple molecular orbital picture. Consideration of the octahedral coordination of Ti by oxygen atoms indicates that there are two unfilled antibonding orbitals, $3t_{2g}$ ($d\pi^*$) and $3e_g$ ($d\sigma^*$) with mainly Ti d-character. Since these hybridized orbitals are also made up from oxygen π^* and σ^* orbitals we expect to see the same levels in the ls$\rightarrow$p transitions. But this simple molecular orbital approach does not give any indication of the energy level spacing. In the case of TiO_2 an extended Hückel tight binding cluster calculation has been used to obtain the density-of-states (Grunes et al., 1982) and this is shown in Fig. 8. The calculated splitting of the $d\pi^*$ and $d\sigma^*$ bands is ~ 3.8 eV which is somewhat higher than the measured value but the theory at least gives a semi-quantitative interpretation of the spectra.

Let us now compare the Ti L_{23} edge in the metal with that from TiO_2. Fig. 9 shows the L_{23} edges in both samples (Leapman and Grunes, 1980). A spin-orbit splitting of 6 eV

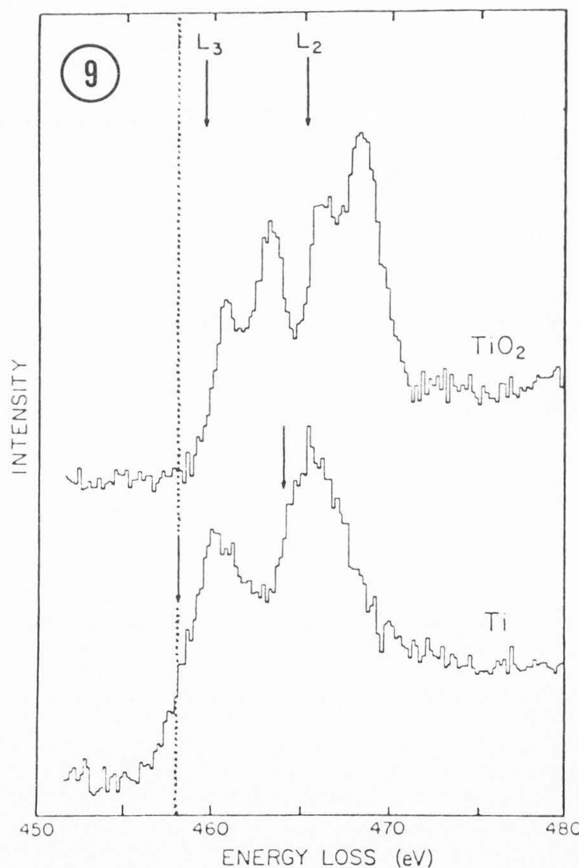

Fig. 9. Comparison of the Ti L_{23} edge from evaporated Ti and from TiO_2 prepared by oxidation of the metal. Arrows correspond to edge thresholds.

between the $2p_{3/2}$ (L_3) and $2p_{1/2}$ (L_2) levels is observed. In the metal and oxide the edge shape is dominated by a strong peak arising from transitions to unoccupied 3d states. The expected ratio of L_3/L_2 intensities is 2:1 and it is not yet clear why the observed ratio in Fig. 9 is nearer 1:1 (Leapman and Grunes, 1980). It seems that some many-electron effect is present. In the metal only one maximum is visible at each of the L_3 and L_2 edges while the oxide displays double maxima as described above. A "chemical shift" of about 2 eV is also evident between the metal and the oxide. This is similar to that observed in x-ray photoemission spectra (XPS) where the shift can be attributed to charge transfer from the metal to oxygen atoms, with a concomitant increase in binding energy. A detailed analysis however indicates that the XPS chemical shift is several eV greater than the EELS chemical shift, after a correction has been made for the band gap separating the occupied and unoccupied states (XPS only involves the occupied levels). The discrepancy can be explained in part by the effect of the core hole on the final states (core exciton) and by relaxation effects.

Significant differences are also observed in the L_{23} edges from copper and copper oxide shown in Fig. 10 (Leapman et al., 1982). In the metal the d-states are completely filled so there is no sharp peak at threshold. In the oxide some of the d-states become unoccupied and intense narrow peaks are visible at L_3 and L_2 edges. The chemical shift in the oxide is in fact negative, suggesting again the importance of excitonic effects.

An understanding of the fine structure thus depends heavily on good band structure computations being available and this is not, in general, the case. For simple solids agreement with theory seems reasonable, while no data is available for the majority of materials. The situation is further complicated by atomic and many-electron effects.

Momentum transfer and orientation dependence

In a crystalline material the core edge fine structure is capable of providing more detailed information about the chemical bonding. For example the momentum transfer dependence of the core edges can be used to investigate anisotropy in the chemical bonding and band structure (Kincaid et al., 1978; Leapman and Silcox, 1979). This dependence occurs because the momentum transfer $\underline{q}$ can be aligned with different excited crystal wave functions in the dipole matrix element in Equation 9. Using the expansion of the operator in Equation 12 in the dipole limit we have a matrix element, $q < f \mid \hat{\epsilon}_q \cdot \underline{r} \mid i >$. Figure 11 shows the spectrum near the carbon K edge from a graphite sample oriented with the c-axis parallel to the incident beam for different scattering angles or momentum transfers. When Θ is small, $\underline{q}$ is along the c-axis and transitions to π^* anti-bonding states (orbitals perpendicular to the layer planes) are strongly favored. When Θ is large the $1s \rightarrow \pi^*$ transitions become weak while transitions to σ^* states (sp^2 hybridized) become dominant. We are thus able to identify the 285.5 eV peak in Figure 11 as a $1s \rightarrow \pi^*$ transition and the peak at 292.5 eV as a $1s \rightarrow \sigma^*$ transition. This assignment is in reasonable agreement with band structure determinations. However the effect of the core hole exciton appears to modify the edge shape compared with that predicted by the one-electron density-of-states and also causes a peak shift to lower energies (Mele and Ritsko, 1979). Instead of varying the scattering angle, similar changes in the spectrum can be obtained by varying the crystal orientation while keeping Θ fixed.

The near edge fine structure can also be exploited to yield structural information in another way as has been recently demonstrated by Taftø and Krivanek (1982). When an electron is incident on a crystal the wavefield becomes modulated inside the crystal unit cell and different Bloch waves are set up. Depending on the incident beam direction with respect to the sample, Bloch wave maxima can be located on or between particular atom or crystal sites. Features in the core loss spectrum may therefore depend on the particular diffracting conditions that are set up. Taftø and Krivanek (1982) have obtained data from a chromite spinel containing iron atoms distributed 3:1 between tetrahedral and octahedral sites. In addition some of the iron atoms were Fe^{2+} and some Fe^{3+} but the distribution of these between the different sites was unknown. Fig. 12 shows these authors' recorded spectrum in the region of the Fe L_{23} edge under two specific diffraction conditions. In the upper curve the octahedral sites are selected and in the lower curve the tetrahedral sites. The double maxima separated by 2 eV can be mainly attributed to the chemical shift between Fe^{2+} and Fe^{3+} ions, the Fe^{2+} energy being the lower. Taftø and Krivanek (1982) thus deduce that the tetrahedral sites contain Fe^{2+} ions while the octahedral sites contain Fe^{3+}.

Extended fine structure

The extended energy loss fine structure (EXELFS) which occurs in the region up to several hundred eV above a core edge can be analyzed in the same way as extended x-ray absorption fine structure (EXAFS) by using the formulation of Stern, Sayers and Lytle (1975). This technique has been shown to yield information about the local environment around a particular atomic species. The weak EXELFS modulations which are typically only a few percent of the background can be considered to arise from interference between the outgoing ejected electron with parts of the electron wave that are backscattered by neighboring atoms. The cross section for ionization depends on the overlap of the core wavefunction with the final state so this contains the oscillatory term. If the wavevector of the ejected electron is k then,

$$\hbar k = [2m(E - E_X)]^{1/2} \qquad 27$$

where E_X is the edge energy and E is the energy loss. The oscillatory part of the spectrum as function of k can be written as,

$$\chi(k) = \frac{1}{k} \sum_j \frac{N_j}{R_j^2} f_j(k) A(k) \sin(2kR_j + \varnothing_j(k)) \qquad 28$$

Summation in Equation 28 is over the j different coordination shells at radius $R_j(k)$ each containing $N_j(k)$ atoms surrounding the excited atom. The backscattering amplitude function $f_j(k)$ depends on the type of atom. The factor A (k) takes account of the range of the ejected electron and thermal vibrations. The phase shift $\varnothing_j(k)$ has two parts, one due to the potential of the excited atom and the other due to the backscattering atom.

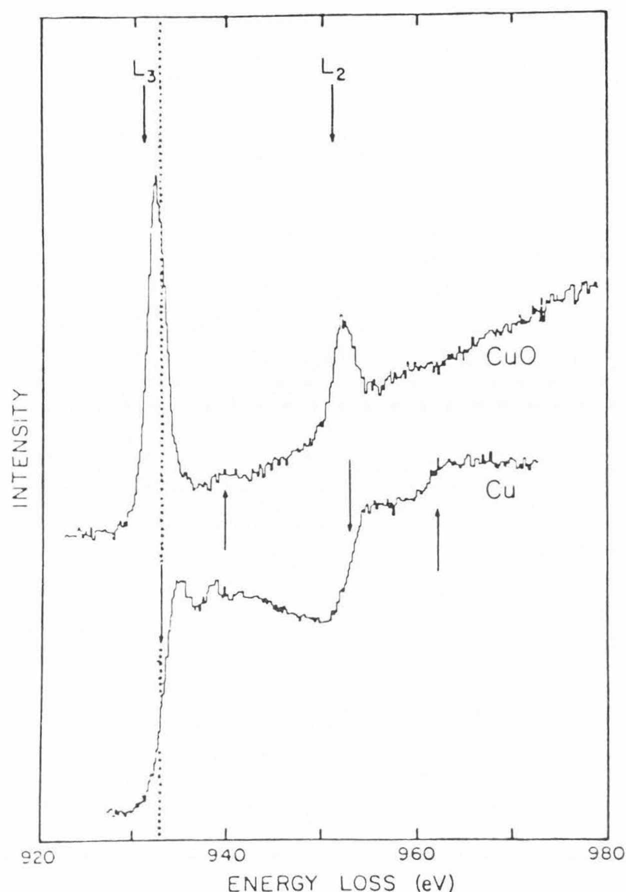

Fig. 10. **Comparison of the Cu L_{23} edge from evaporated Cu and from CuO prepared by oxidation of the metal. Downward arrows correspond to edge thresholds, upward arrows to subsidiary features in the fine structure.**

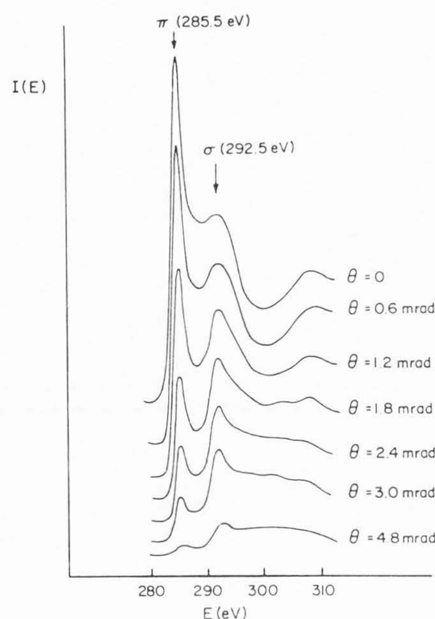

Fig. 11. **Carbon K edge in graphite (c-axis in the beam direction) at different values of scattering angle Θ. The curves were obtained from microdensitometer traces across a photographic plate. Data were collected with a retarding field Wien filter spectrometer combined with a CTEM operating in the diffraction mode (Leapman and Silcox, 1979). A range of scattering angles was selected by an entrance slit to the spectrometer which dispersed the electrons in a perpendicular direction. The resulting pattern was recorded on film.**

EXELFS spectroscopy has two significant advantages over the conventional EXAFS. It can be applied to light elements whereas the x-ray absorption technique has run into difficulties in the soft x-ray energy range, and it can be applied to microscopic areas of thin samples while EXAFS is essentially a bulk method (Leapman and Cosslett, 1976; Batson and Craven, 1979; Leapman et al. 1981; Csillag et al., 1981; Disko, 1981). In fact Isaacson and Utlaut (1978) and Kincaid et al. (1978) have established that electrons might provide a superior probe to x-rays in the energy range of a few hundred eV where the K edges of the light elements occur. It is noted that a new EXAFS technique relying on the secondary electron yield has been developed, and this is capable of producing data at lower energies than the conventional EXAFS (Stöhr, 1979). Nevertheless this is a surface tool and applies to a different type of sample.

Since EXELFS can be carried out in the electron microscope a sample can be characterized by diffraction and high resolution imaging at the same time. In particular EXELFS spectroscopy is expected to be a useful probe for amorphous materials where these alternative techniques cannot give complete information. We show in Fig. 13 the core edges

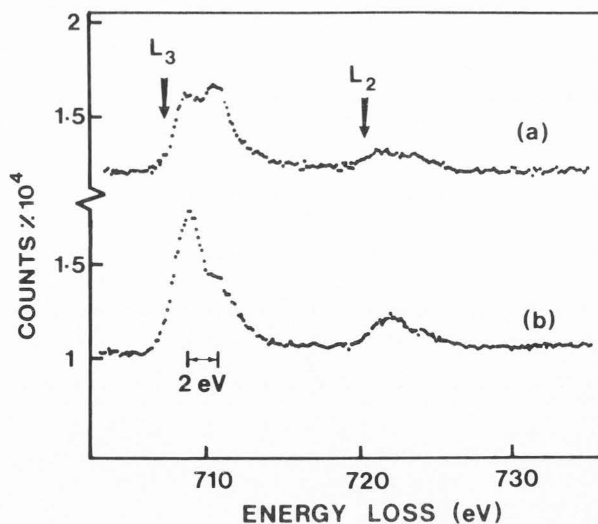

Fig. 12. **Detailed structure at the iron L_{23} edge in chromite recorded by Taftø and Krivanek (1982) for two different orientations of the crystal. In (a) octahedral sites are selected and in (b) tetrahedral sites.**

from a sample of amorphous silicon nitride recorded at 200 keV beam energy from a sample about 100 nm thick.

As a first step to analyzing the data we have deconvoluted the core edges using the low loss spectrum according to Equation 24 . The background-subtracted nitrogen K edge (400 eV) and the Si K edge (1840 eV) as well as the low loss spectrum are shown in Fig. 13. The sample thickness estimated from Equation 18 is $1.1\lambda_T$. Next, the intensity is changed from a function of E to a function of k and a third order polynomial is carefully fitted through the data. Then the resulting modulations are multiplied by k^3 to take account of attenuation by the backscattering amplitude function. After choosing a suitable range of k_{min} to k_{max}, the data is Fourier transformed to give the radial distribution function. The limit k_{min} is chosen as about 3 $Å^{-1}$ below which near-edge effects due to the solid are important. The upper limit k_{max} is determined by noise or the interference of another edge, and is typically 10 $Å^{-1}$. Finally a correction must be made for the phase shift; we have made use of the calculations of Teo and Lee (1979) and estimate only the linear part here. This value is simply added on to the peak positions in the radial distribution function as prescribed by Equation 28 .

Figure 14 shows the computed radial distribution function for silicon nitride for both nitrogen and silicon atoms. Nearest neighbor peaks occur at 1.38 Å for both types of atom and a second weak peak is visible at 2.7 Å. After correction for the phase shift of 0.40 Å, the nearest and second nearest neighbor distances are 1.78 ± 0.07 Å and 3.1 ± 0.1 Å respectively. This is in agreement with existing x-ray diffraction data where the Si-N bond length was determined as 1.75 Å, and the second nearest correlation distance for Si-Si and N-N as 3.0 Å (Aiyama et al., 1979). Silicon is tetrahedrally coordinated with four nitrogen atoms and nitrogen is coordinated with three silicon atoms as shown in Fig. 14.

So far attempts have only been made to demonstrate the feasibility of EXELFS analysis and the technique has not yet been used to solve unknown structures. EXELFS spectroscopy relies on good statistics to obtain a useful k-range preferably up to 10 or 12 $Å^{-1}$. Such data should be obtainable with improved spectrometer optics and detection systems.

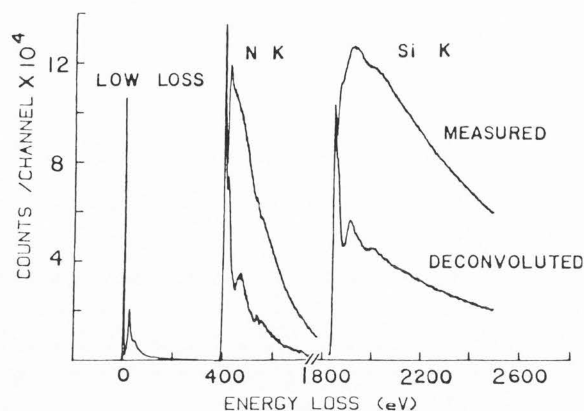

Fig. 13. Low loss and core edge spectra from amorphous silicon nitride. Measured and deconvoluted K edges for N and Si are shown.

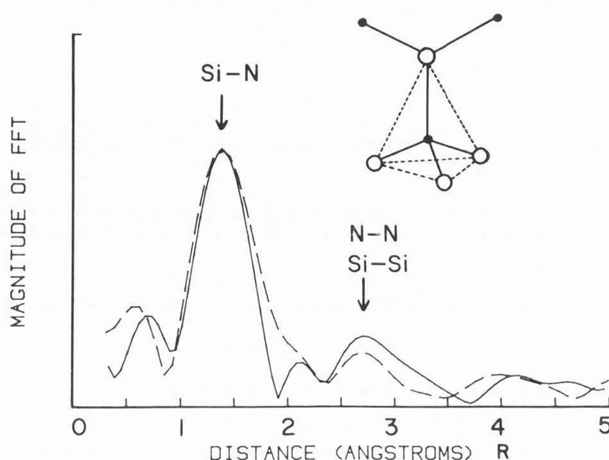

Fig. 14. Radial distribution function for Si (solid line) and N (dashed line) showing peaks at 1.38 Å and 2.7 Å. Coordination of nitrogen (open circles) around silicon (closed circles) is indicated.

SUMMARY AND COMMENTS

We have tried to describe the wide range of information that is contained in the electron energy loss spectrum and to discuss some of the different ways in which it can be analyzed. The low loss spectrum, which we only considered briefly, is very rich in structure provided the energy resolution is sufficient (≤0.5 eV). Interpretation of the data generally requires some prior knowledge about the sample. Often sophisticated methods must be employed for data collection and analysis. Extremely valuable information can then be derived about the electronic structure. As yet only a few attempts have been made to extend such experiments to very small dimensions but this should certainly be possible as has been discussed by Isaacson (1981).

The core edges give important information about the elemental composition which can be obtained with a relatively straightforward analysis provided edge overlap does not occur. Detection limits appear to be very low, perhaps a few atoms if a field emission source is used. This low limit of detectability suggests that high resolution core loss imaging might be feasible and this is supported by the estimated high degree of localization of the excitation processes. Precise quantitative analysis is more difficult. Quantitation for K and L edges appears to be now possible with reasonable accuracy (about ±10%) but there is still some uncertainty about the cross sections for M and N shells.

A fruitful area of exploration concerns the fine structure near the core edges. We have demonstrated some of the different types of information about chemical bonding, band structure and local atomic environment that can be extracted. A considerable amount of theoretical work is required to explain all the observed features in the spectrum satisfactorily. Nevertheless, while a few years ago we were discussing the possibility of microanalysis on a nanometer scale, we are now considering the possibility of determining the electronic structure at the same dimensions.

REFERENCES

Aiyama T, Fukanaga T, Nihara K, Hirai T and Suzuki K. (1979). An x-ray diffraction study of the amorphous structure of chemical vapor deposited silicon nitride. J. Non-Cryst. Solids. **33**, 131-139.

Batson PE, Chen CH and Silcox J. (1976). Plasmon dispersion at large wavevectors in aluminun. Phys. Rev. Lett. **37**, 937-940.

Batson PE. (1976). An experimental determination of the form factor S(q,ω) for the valence electrons in aluminum, PhD thesis, Cornell University, Ithaca, N.Y.

Batson PE and Craven AJ. (1979). Extended fine structure on the carbon core ionization edge. Phys. Rev. Lett. **42**, 893-896.

Bethe H. (1930). Zur Theorie des Durchgangs schneller Korpuskularstrahlen durch Materie. Ann. Physik **5**, 325-400.

Brown FC. (1974). Ultraviolet spectroscopy of solids with the use of synchrotron radiation. Solid State Physics. **29**, 1-73.

Brown LM. (1981). Scanning transmission electron microscopy: microanalysis for the electronic age. J. Phys. F**11**, 1-26.

Brousseau-Lahaye B, Colliex C, Frandon J, Gasgnier M and Trebbia P. (1975). Determination of the electron excitation spectrum in scandium and yttrium by means of characteristic energy loss measurements. Phys. Stat. Sol. b**69**, 257-266.

Castaing R and Henry L. (1962). Filtrage magnetique des vitesses en microscopie électronique. Comptes Rendu. Acad. Sci. Paris, B**255**, 76-80.

Chen CH and Silcox J. (1975). Detection of optical surface guided modes in thin graphite films by high energy electron scattering. Phys. Rev. Lett. **35**, 390-393.

Chen CH, Silcox J and Vincent R. (1975). Electron energy losses in silicon: bulk and surface plasmons and Cerenkov radiation. Phys. Rev. B**12**, 64-71.

Chen CH and Silcox J. (1977). Direct non-vertical interband transitions at large wavevectors in aluminum. Phys. Rev. B **16**, 4246-4248.

Colliex C and Jouffrey B. (1972). Diffusion inélastique des electron dans un solide par excitation de niveaux atomiques profonds. Phil. Mag. **25**, 491-511.

Colliex C and Trebbia P. (1978). Electron energy loss spectroscopy in the electron microscope: present state of affairs., In: Electron Microscopy, Toronto, J.M. Sturgess (Ed.), Microscopical Society of Canada (publisher),3, 268-279.

Colliex C, Cosslett VE, Leapman RD and Trebbia P. (1976). Contribution of electron energy loss spectroscopy to the development of analytical electron microscopy. Ultramicroscopy **1**, 301-315.

Crewe AV, Isaacson M and Johnson DE. (1971). A high resolution electron spectrometer for use in transmission scanning electron microscopy. Rev. Sci. Instrum. **42**, 411-420.

Csillag S, Johnson DE and Stern EA. (1981). Extended energy loss fine structure studies in an electron microscope, In: EXAFS Spectroscopy: Techniques and Applications, B.K. Teo and D.C. Joy (Eds.), Plenum Press, N.Y., p. 241-254.

Curtis GH and Silcox J. (1971). A Wien Filter for use as an energy analyzer with an electron microscope. Rev. Sci. Instrum. **42**, 630-637.

Daniels J, Festenberg Cv, Raether H and Zeppenfeld D. (1970). Optical constants of solids by electron spectroscopy. Springer Tracts in Modern Physics (Berlin: Springer Verlag) **54**, 77-135.

Disko MM. (1981). An EXELFS analysis system and the preliminary orientation dependence of EXELFS in graphite, In: Analytical Electron Microscopy, R.H. Geiss (Ed.), San Francisco Press, p. 214-220.

Egerton RF and Whelan MJ. (1974a). High resolution microanalysis of light elements by electron energy loss spectroscopy. Proc. 8th Int. Cong. on Electron Microscopy (Canberra: Australian Acad. Sciences) **1**, 384-385.

Egerton RF and Whelan MJ. (1974b). The electron energy loss spectrum and band structure of diamond. Phil. Mag. **30**, 739-749.

Egerton RF and Whelan MJ. (1974c). Electron energy loss spectra of diamond, graphite and amorphous carbon. J. Electron Spectroscopy and Related Phenomena **3**, 323-336.

Egerton RF. (1975). Inelastic scattering of 80 keV electrons in amorphous carbon. Phil. Mag. **31**, 199-215.

Egerton RF. (1978). Quantitative energy loss spectroscopy, Scanning Electron Micros. 1978; I: 133-142.

Egerton RF. (1979). K-shell ionization cross sections for use in microanalysis. Ultramicroscopy **4**, 169-179.

Egerton RF. (1980a). Design of an aberration corrected electron spectrometer for TEM. Optik **57**, 229-242.

Egerton RF. (1980b). Instrumentation and software for energy loss microanalysis, Scanning Electron Micros. 1980; I: p. 41-52.

Egerton RF. (1981a). Design of a parallel detection system for EELS. Proc. 39th EMSA Conf., G.W. Bailey (Ed.), Claitor's Publishing,Baton Rouge, p. 368-369.

Egerton RF. (1981b). SIGMAL: A program for calculating L-shell ionization cross sections. Proc. 39th EMSA Conf., G.W. Bailey (Ed.), Claitor's Publishing, Baton Rouge, p. 198-199.

Grunes LA and Leapman RD. (1980). Optically forbidden excitations of the 3s subshell in the 3d transition metals by inelastic scattering of fast electrons. Phys. Rev. B **22**, 3778-3783.

Grunes LA, Leapman RD, Wilker CN, Hoffman R and Kunz AB. (1982). Oxygen K near edge fine structure: An electron energy loss investigation with comparison to new theory for selected 3d transition metal oxides. Phys. Rev. B **25**, 7157-7173.

Hillier J and Baker RF. (1944). Microanalysis by means of electrons. J. Appl. Phys. **15**, 663-676.

Howie A. (1981). Localization and momentum transfer in inelastic scattering. Proc. 39th EMSA Conf., G.W. Bailey (Ed.), Claitor's Publishing, Baton Rouge, p. 186-189.

Inokuti M. (1971). Inelastic collisions of fast charged particles with atoms and molecules: the Bethe theory revisited. Rev. Mod. Phys. **43**, 297-347.

Isaacson M. (1972). Interactions of 25 keV electrons with the nucleic acid bases, adenine, thymine and uracyl: II. Inner-shell excitations and inelastic cross sections. J. Chem. Phys. **56**, 1813-1818.

Isaacson M and Johnson DE. (1975). The microanalysis of light elements using transmitted energy loss electrons. Ultramicroscopy **1**, 33-52.

Isaacson M and Utlaut M. (1978). A comparison of electron and photon beams for determining microchemical environment. Optik **50**, 213-234.

Isaacson M, Collins ML and Listvan M. (1978). Electron beam damage of biomolecules assessed by electron energy loss spectroscopy, In: Electron Microscopy, Toronto, J.M. Sturgess (Ed.), Microscopical Society of Canada, **3**, p. 61-69.

Isaacson M. (1980). A poor man's approach to semi-quantitative analysis with electron energy loss spectroscopy. Proc. 38th EMSA Conf., G.W. Bailey (Ed.), Claitor's Publishing, Baton Rouge, p. 110-111.

Isaacson M. (1981). The potential of energy loss spectroscopy for electronic characterization of structures on the nanometer scale. Ultramicroscopy **7**, 55-58.

Johnson DE. (1979). Basic aspects of energy loss spectrometer systems. Ultramicroscopy **3**, 361-365.

Johnson DE. (1980). Pre-spectrometer optics in a CTEM/STEM. Ultramicroscopy, **5**, 163-174.

Johnson DE, Monson KL, Csillag S and Stern EA. (1981). An approach to parallel detection electron energy loss spectrometery, In: Analytical Electron Microscopy, R.H. Geiss (Ed.), San Francisco Press, p. 205-209.

Johnson DW and Spence JC. (1974). Determination of the single scattering distribution from plural scattering data. J. Phys. D. **7**, 771-780.

Jouffrey B and Sevely J. (1976). Utilization en microscopie électronique des pertes d' energie des electrons pour l'analyse chimique locale. Revue Phys. Appliquee **11**, 101-111.

Jouffrey B, Kihn Y, Perez J. Ph, Sevely J and Zanchi G. (1978). On chemical analysis of thin films by energy loss spectroscopy, In: Electron Microscopy, Toronto, J.M. Sturgess (Ed.), Microscopical Society of Canada, **3**, p. 292-303.

Joy DC and Maher DM. (1978a). A practical electron spectrometer for chemical analysis. J. Microscopy **114**, 117-130.

Joy DC and Maher DM (1978b). The choice of operating parameters for microanalysis by electron energy loss spectroscopy. Ultramicroscopy **3**, 69-74.

Joy DC. (1979). The basic principles of electron energy loss spectroscopy, In: Introduction to Analytical Electron Microscopy, J.J. Hren, J.L. Goldstein and D.C. Joy (Eds.), Plenum Press, N.Y., p. 223-244.

Joy DC, Egerton RF and Maher DM. (1979). Progress in the quantitation of energy loss spectra, Scanning Electron Microsc. 1979; II: p. 817-826.

Joy DC and Maher DM. (1980). Electron energy loss spectroscopy: detection limits for elemental analysis. Ultramicroscopy **5**, 333-342.

Joy DC and Maher DM. (1981). The quantitation of ELS. J. Microscopy **124**, 37-48.

Kincaid BM, Meixner EA and Platzman PM. (1978). Carbon K edge in graphite measured using electron energy loss spectroscopy. Phys. Rev. Lett. **40**, 1296-1299.

Krivanek OL. (1979). Design of a compact, medium resolution electron energy loss spectrometer. Proc. 37th EMSA Conf., G.W. Bailey (Ed.), Claitor's Publishing, Baton Rouge, p. 530-531.

Krivanek OL. (1980). Application of electron energy loss spectroscopy in materials science. Proc. 38th EMSA Conf., G.W. Bailey (Ed.), Claitor's Publishing, Baton Rouge, p. 86-89.

Leapman RD and Cosslett VE. (1976). Extended fine structure above the x-ray edge in electron energy loss spectra. J. Phys. D. **9**, L26-L29.

Leapman RD and Silcox J. (1979). Orientation dependence of core edges in electron energy loss spectra from anisotropic materials. Phys. Rev. Lett. **42**, 1361-1364.

Leapman RD. (1979). Energy loss spectroscopy of core excitations and quantitative microanalysis. Ultramicroscopy **3**, 413-421.

Leapman RD and Grunes LA. (1980). Anomalous L_{23} white line intensity ratios in the 3d transition elements. Phys. Rev. Lett. **45**, 397-401.

Leapman RD, Rez P and Mayers DF. (1980). K, L and M shell generalized oscillator strengths and ionization cross sections for fast electron collisions. J. Chem. Phys. **72**, 1232-1241.

Leapman RD, Grunes LA, Fejes PL and Silcox J. (1981). Extended core edge fine structure in electron energy loss spectra, In: EXAFS Spectroscopy: Techniques and Applications, B.K. Teo and D.C. Joy (Eds.), Plenum Press Press, N.Y, p. 217-240.

Leapman RD and Swyt CR. (1981). Electron energy loss spectroscopy under conditions of plural scattering, In: Analytical Electron Microscopy, R.H. Geiss (Ed.), San Francisco Press, p. 164-172.

Leapman RD, Grunes LA and Fejes PL. (1982). A study of the L_{23} edges in the 3d transition metals and their oxides by electron energy loss spectroscopy with comparisons to theory. Phys. Rev. B **26**, 614-635.

Leapman RD. (1982). Applications of electron energy loss spectroscopy in biology: Detection limits for calcium and fluorine. Proc. EMSA Conf., G.W. Bailey (Ed.), Claitor's Publishing, Baton Rouge, p. 412-415.

Maher DM. (1979). Elemental analysis using inner-shell excitations: A microanalytical technique for materials characterization, In: Introduction to Analytical Electron Microscopy, J.J. Hren, J.L. Goldstein and D.C. Joy (Eds.), Plenum Press, NY, p. 259-294.

Manson ST. (1972). Inelastic scattering of fast charged particles with atoms: ionization of the aluminum L-shell. Phys. Rev. A **6**, 1013-1024.

Mele EJ and Ritsko JJ. (1979). Fermi level lowering and the core excitation spectrum of intercalated graphite. Phys. Rev. Lett. **43**, 68-71.

Pines D. (1964). Electrons and Plasmons, In: Elementary Excitations in Solids, Benjamin, N.Y., Chapter 3, p. 56-167.

Powell CJ. (1976). Cross sections for ionization of inner-shell electrons by electrons. Rev. Mod. Phys. **48**, 33-47.

Ray AB. (1981). Electron energy loss study of the optical properties of anisotropic thin film boron nitride, Ph.D. thesis, Cornell University, Ithaca, N.Y.

Rez P and Leapman RD. (1981). Core loss shape and cross section calculations, In: Analytical Electron Microscopy, R.H. Geiss (Ed.), San Francisco Press, p. 181-186.

Ritsko JJ and Mele EJ. (1980). Experimental determination of the momentum-dependent dielectric response of stage-1 $FeCl_3$ – intercalated graphite. Phys. Rev. B **21**, 730-738.

Rossouw CJ, Egerton RF and Whelan MJ. (1977). Applications of energy analysis in a transmission electron microscope. Vaccum **26**, 427-432.

Schnatterly SE. (1979). Inelastic electron scattering spectroscopy. Solid State Physics **34**, 275-357.

Shuman H. (1980). Correction of the second-order aberrations of uniform field magnetic sectors. Ultramicroscopy **5**, 45-53.

Shuman H. (1981). Parallel recording of electron energy loss spectra. Ultramicroscopy **6**, 163-167.

Silcox J. (1978). Inelastic electron-matter interactions, In: Electron Microscopy, Toronto, J.M. Sturgess (Ed.), Microscopical Society of Canada,**3**, 259-267.

Stern EA, Sayers DE and Lytle FW. (1975). Extended x-ray absorption fine structure technique: Determination of physical parameters. Phys. Rev. B **11**, 4836-4846.

Stöhr J. (1979). EXAFS and surface EXAFS studies in the soft x-ray region using electron yield spectroscopy. J. Vac. Sci. Technol. **16**, 37-41.

Taftø J and Krivanek OL. (1982). Site-specific valence determination by electron energy loss spectroscopy. Phys. Rev. Lett. **48**, 560-563.

Teo BK and Lee PA. (1979). Ab initio calculations of amplitudes and phases functions for EXAFS spectroscopy. J. Am. Chem. Soc. **101**, 2815-2832.

Trebbia P and Colliex C. (1973). Study of the excitation of 4 d electrons in rare-earth metals by inelastic scattering of a high energy electron beam. Phys. Stat. Sol. b **58**, 523-531.

Watanabe H. (1955). Energy analysis of electron diffraction patterns. J. Phys. Soc. Jap. **10**, 321-323.

Williams DB and Edington JW. (1976). High resolution microanalysis in materials science using electrons energy loss measurements. J. Microscopy **108**, 113-145.

Wittry DB. (1969). An electron spectrometer for use with the transmission electron microscope. Brit. J. Appl. Phys. **2**, 1957-1966.

Wittry DB, Ferrier RP and Cosslett VE. (1969). Selected area electron spectrometry in the electron microscope. Brit. J. Appl. Phys. **2**, 1967-1973.

Zanchi G, Sevely J and Jouffrey B. (1977). An energy filter for high voltage electron microscopy. J. Microscopie et Spectroscopie Electronique **2**, 95-104.

WRITTEN DISCUSSION

R. Shimizu: Can surface plasmon peaks be observed in ELS in the 10^{-6} Torr Region? What excitation is responsible for the small peak at a 16 eV in the spectrum of BeO in Fig. 2?

Author: Surface plasmon peaks can be observed under these conditions especially in thin samples. In fact a detailed analysis of the bulk and surface plasmon excitations in aluminum has been given by Batson [ref. in text]. The surface plasmon is generally observed at an energy

$$\frac{1}{\sqrt{2}}$$

that of the bulk plasmon excitation and this was measured together with the dispersion as a function of $\underline{q}$ in the case of aluminum. The origin of the 16 eV peak in the BeO spectrum is not certain. There may be some contribution from the Be metal since the BeO precipitate may not occupy the entire thickness of the sample. However, the peak is somewhat lower in energy than the Be plasmon and may therefore be attributed in part to a single electron or collective excitation in the oxide, separate from the 25 eV excitation.

R. Shimizu: Concerning Equation 17, is it not in principle necessary to use a plasmon peak profile, $I_{PL}(E) = -\omega^{-1} \operatorname{Im}[(\epsilon+1)^{-1}]$ which has for example a width of ~ 1 eV for Al from a simple estimation using optical constant measurements and a slightly larger value for Si, instead of $\delta(E)$ because this value is no more negligible in the evaluation of final peak profile observed?

Author: In Equation 17, the δ-function only refers to electrons which have not been inelastically scattered. The width of the plasmon peak is incorporated into the single scattering distribution Q(E). If the momentum transfer dependence is ignored, Equation 17 is exact. Of course, the $\underline{q}$-dependence is important for a detailed understanding of the inelastic scattering and Equation 17 must be adapted as mentioned in the text.